An ALE formulation for implicit time integration of quasi-steady-state wear problems

Stanisław Stupkiewicz*

Institute of Fundamental Technological Research (IPPT)
Pawińskiego 5B, 02–106 Warsaw, Poland

Abstract

A fully coupled implicit scheme is developed for quasi-steady-state wear problems. The formulation admits finite configuration changes due to both deformation and wear. The unconditionally stable implicit backward-Euler scheme is used for time integration of the shape evolution problem. Thus, the solution may proceed with large time increments, contrary to the commonly used explicit forward-Euler scheme, in which the time increment is restricted by the stability condition. This comes at the cost that the shape transformation mapping constitutes an additional unknown. As a result, a kind of an arbitrary Lagrangian-Eulerian (ALE) formulation is obtained in which the problem is solved simultaneously for the nodal positions and displacements. The incremental coupled problem is solved using the Newton method which leads to a highly efficient computational scheme, as illustrated by two- and three-dimensional numerical examples.

Keywords: contact, wear, shape evolution, arbitrary Lagrangian-Eulerian formulation, automatic differentiation

1. Introduction

Wear is a process of material removal from a surface subjected to frictional contact interaction. Wear processes are usually slow, and noticeable effects result from repeated contacts and accumulation of wear over a long period. Simulation of this class of contact problems is a challenging task as it involves shape changes due to accumulated wear and the associated evolution

*Email address: sstupkie@ippt.gov.pl

of the contact zone, pressure, etc. This work is concerned with computational modelling of progressive wear, and the adopted approach belongs to the class of incremental solution strategies. Note that alternative direct approaches have been developed for asymptotic or steady-state wear processes, cf. [1–4].

The incremental solution procedures for progressive wear problems are usually based on the explicit forward-Euler time integration scheme. Specifically, at each time step, the contact problem is solved for the known current shape of the contacting bodies, and the wear rate is computed as a postprocessing quantity. The wear depth increment is then obtained by multiplying the wear rate by the time increment, the shape is updated accordingly, and the solution proceeds to the next time step. This procedure has been used in combination with the finite element method [5–11] and the boundary element method [12–14]; specialized contact solvers have also been developed for that purpose [15, 16]. A more accurate second-order explicit integration scheme has been recently developed in [11] which exploits shape sensitivity analysis [17]. When finite configuration changes due to wear are considered, the shape update necessarily involves remeshing [6–11, 13]. Alternatively, assuming that the shape changes are small, and adopting the small-deformation framework, the shape change can be introduced by simply adding the wear depth to the initial normal gap [5, 12, 14].

The explicit forward-Euler scheme is simple and quite straightforward to implement, hence its popularity in modelling of progressive wear. However, as it is well known, this scheme is only conditionally stable, and the related instabilities are commonly encountered in computational practice [5–8, 11, 13]. It has been shown in [5] that the critical time increment decreases with increasing elastic modulus and with decreasing element size. The latter effect implies that mesh refinement increases the computational cost both due to the increased number of unknowns and due to the increased number of time steps. Thus, in problems of practical interest, the solution may be prohibitively expensive due to the stability condition enforced on the time increment.

On the contrary, the implicit backward-Euler scheme is unconditionally stable so that the time increment is constrained only by the desired accuracy of the solution. Application of the implicit scheme requires that the wear increment (or shape transformation resulting from wear) constitutes an additional unknown in the problem. In the context of wear evolution problems, the implicit time integration scheme has, so far, been employed only by Strömberg [18], Jourdan and Samida [19], and Ben Dhia and Torkhani

[20]. In the small-deformation framework adopted in [18], the configuration changes are neglected, and the wear depth is an additional unknown that is added to the initial normal gap. The formulations adopted in [19, 20] admit finite deformations and finite configuration changes due to wear. In [19], the shape transformation due to wear is restricted to the outer layer of elements only, and the computational treatment is derived from the non-smooth contact dynamics method [21]. The resulting finite-element equations are not fully linearized so that the iterative solution scheme is effectively a modified Newton method. In the implicit scheme developed in [20], the coupled wear–deformation problem is not fully linearized either, and the shape transformation is determined using a fixed-point iteration method.

In this work, a fully coupled implicit scheme is developed for quasi-steady-state wear problems. The finite-deformation formulation of the contact and wear problem follows that recently developed by Lengiewicz and Stupkiewicz [11]. Finite configuration changes due to both deformation and wear are consistently described by introducing three configurations and the corresponding mappings: the shape transformation mapping and the deformation mapping. Both mappings constitute the unknowns of the problem. The deformation mapping is governed by the usual mechanical equilibrium equations including the contact interaction, and the shape transformation mapping is determined from an auxiliary elasticity problem which is driven by wear increments on the contact boundary. As a result, a kind of an arbitrary Lagrangian-Eulerian (ALE) formulation is obtained in which the shape transformation (i.e., the mesh motion in the finite element context) is resolved simultaneously with the displacements, all in a fully implicit manner. The resulting finite-element equations are solved using the Newton method, and its quadratic convergence is achieved thanks to full linearization of the governing equations. Two- and three-dimensional numerical examples illustrate the benefit of applying the implicit time integration scheme in wear evolution problems.

2. Continuum formulation

2.1. General finite-wear problem: three configurations and two time scales

Consider two hyperelastic bodies $\mathcal{B}^1$ and $\mathcal{B}^2$ subjected to frictional contact and wear. Following the continuum formulation proposed in [11], three configurations of $\mathcal{B}^i$ are introduced: the initial configuration $\hat{\Omega}^i$, the time-dependent undeformed configuration Ω^i, and the current (deformed) configuration ω^i. The shape change due to wear is described by the *shape trans-*

formation mapping $\boldsymbol{\Psi}^i$, and the deformation is described by the *deformation mapping* $\boldsymbol{\varphi}^i$, so that

$$\boldsymbol{X}^i = \boldsymbol{\Psi}^i(\hat{\boldsymbol{X}}^i, t), \qquad \boldsymbol{x}^i = \boldsymbol{\varphi}^i(\boldsymbol{X}^i, t), \qquad t \in [0, T], \tag{1}$$

where $\hat{\boldsymbol{X}}^i \in \hat{\Omega}^i$, $\boldsymbol{X}^i \in \Omega^i$, $\boldsymbol{x}^i \in \omega^i$. Both the deformation and the shape change due to wear are allowed to result in finite configuration changes. The initial configuration $\hat{\Omega}^i$ is assumed to be a stress-free (natural) configuration. The undeformed configuration Ω^i is thus also a stress-free configuration.

The undeformed configuration Ω^i evolves in time as a result of accumulation of wear at the contact interface. Shape evolution due to wear is governed by

$$\dot{\boldsymbol{\Psi}}^i \cdot \boldsymbol{N}^i = \begin{cases} -\dot{W}^i & \text{on } \hat{\Gamma}^i_c, \\ 0 & \text{on } \hat{\Gamma}^i \setminus \hat{\Gamma}^i_c, \end{cases} \tag{2}$$

where $\hat{\Gamma}^i$ is the boundary of $\hat{\Omega}^i$, $\hat{\Gamma}^i_c \subset \hat{\Gamma}^i$ denotes the potential contact surface, and $\boldsymbol{N}^i$ is the unit outer normal defined in the undeformed configuration Ω^i. The nominal wear rate $\dot{W}^i \geq 0$ in Eq. (2) denotes the wear volume per unit area and unit time, where both the volume and the area refer to the undeformed configuration Ω^i.

Considering that wear is typically a slow process, i.e., the shape and contact conditions change due to slow accumulation of wear, two time scales can be introduced [11], namely the slow t-scale of shape evolution due to wear and the fast τ-scale of the deformation problem. Now, assuming separation of the two time scales, the shape evolution problem and the deformation problem are partially decoupled so that the deformation problem can be analyzed at fixed slow time t, and it becomes a standard contact problem. The shape and deformation mappings are thus rewritten in the form:

$$\boldsymbol{X}^i = \boldsymbol{\Psi}^i(\hat{\boldsymbol{X}}^i, t), \quad \boldsymbol{x}^i = \boldsymbol{\varphi}^i_t(\boldsymbol{X}^i, \tau), \quad t \in [0, T], \quad \tau \in [t, t + \Delta\tau], \tag{3}$$

where $\boldsymbol{X}^i \in \Omega^i_t$, $\Omega^i_t = \boldsymbol{\Psi}^i(\hat{\Omega}^i, t)$, and $\Delta\tau$ is a characteristic time of the deformation problem, for instance, one cycle of a cyclic loading program. The details can be found in [11].

2.2. Quasi-steady-state wear problem

This work is concerned with a special class of wear problems, namely with quasi-steady-state wear problems. In a quasi-steady-state wear problem, the deformation problem corresponding to a fixed slow time t is a steady-state

frictional contact problem once formulated in an appropriate Eulerian frame. Specifically, the Eulerian description is adopted in the reference configuration $\hat{\Omega}^i$ and in the undeformed configuration Ω_t^i to account for the rigid-body motion of one or both contacting bodies, so that the (Lagrangian) deformation mappings $\boldsymbol{\varphi}_t^i$ do not depend on the fast time τ, and we have

$$\boldsymbol{X}^i = \boldsymbol{\Psi}^i(\hat{\boldsymbol{X}}^i, t), \quad \boldsymbol{x}^i = \boldsymbol{\varphi}_t^i(\boldsymbol{X}^i), \quad t \in [0, T], \tag{4}$$

where $\boldsymbol{X}^i \in \Omega_t^i$, $\Omega_t^i = \boldsymbol{\Psi}^i(\hat{\Omega}^i, t)$. Clearly, the deformation problem is parameterized by the slow time t of the shape evolution problem. Typical examples of quasi-steady-state wear problems are the pin-on-disc tribological test and rolling contact. For instance, in the former case, the reference frame is attached to the pin, and the disc is analyzed in an Eulerian frame.

2.3. Steady-state frictional contact problem

Consider a steady-state quasi-static frictional contact problem in which the motion is decomposed into rigid-body motion (in an Eulerian description) and deformation (in a Lagrangian description). As the contacting bodies are hyperelastic, i.e., their behaviour is time- and history-independent, and the inertial effects are neglected, the rigid-body motion in the Eulerian undeformed configuration does not affect the deformation problem, except that relative sliding must be defined properly. As discussed above, the deformation mappings $\boldsymbol{\varphi}_t^i$ do not depend on the fast time τ. To simplify the notation, the dependence on the slow time t, which parameterizes the deformation problem, is not indicated explicitly in this subsection.

The contact formulation adopted in this work is rather standard, and it is briefly introduced below. The details can be found, for instance, in the monographs [22, 23]. A somewhat non-standard part is the Eulerian description of rigid-body motion and the related definition of the tangential sliding velocity, which is, however, straightforward in the present case of a steady-state problem. A more general ALE formulation of transient (non-stationary) rolling contact can be found in [24].

In the master-slave formulation, contact points are associated through the closest-point projection of a point $\boldsymbol{x}^1$ of the deformed slave surface $\gamma_c^1 = \boldsymbol{\varphi}^1(\Gamma_c^1)$ onto the deformed master surface $\gamma_c^2 = \boldsymbol{\varphi}^2(\Gamma_c^2)$. The projection point is denoted by $\bar{\boldsymbol{x}}^2 = \boldsymbol{x}^2(\bar{\boldsymbol{\xi}})$, where the master surface γ_c^2 has been parameterized by convective coordinates $\boldsymbol{\xi} = \{\xi^1, \xi^2\}$, and $\bar{\boldsymbol{\xi}}$ denotes the coordinates of the projection point $\bar{\boldsymbol{x}}^2$.

The normal gap is defined in a standard manner,

$$g_N = (\boldsymbol{x}^1 - \bar{\boldsymbol{x}}^2) \cdot \boldsymbol{n}, \tag{5}$$

where $\boldsymbol{n} = \boldsymbol{n}^2$, and $\boldsymbol{n}^2$ is a unit vector normal to γ_c^2. The tangential sliding velocity is defined as

$$\boldsymbol{v}_T = v_T^\alpha \boldsymbol{\tau}_\alpha, \qquad v_T^\alpha = (\boldsymbol{v}^1 - \bar{\boldsymbol{v}}^2) \cdot \boldsymbol{\tau}^\alpha, \qquad \alpha = 1, 2, \tag{6}$$

where $\boldsymbol{\tau}_\alpha = \partial \boldsymbol{x}^2 / \partial \xi^\alpha$ is the tangent basis, $\boldsymbol{\tau}^\alpha$ is the cobasis, $\boldsymbol{\tau}^\alpha \cdot \boldsymbol{\tau}_\beta = \delta_\beta^\alpha$, $\boldsymbol{v}^i$ denotes the velocity of the material point $\boldsymbol{x}^i$, and $\bar{\boldsymbol{v}}^2 = \boldsymbol{v}^2(\bar{\boldsymbol{x}}^2)$ is the velocity of the projection point $\bar{\boldsymbol{x}}^2$. Considering that the deformation problem is a steady-state problem, velocity $\boldsymbol{v}^i$ results solely from the rigid-body motion with velocity $\boldsymbol{V}^i$ in the undeformed configuration Ω^i, and we have

$$\boldsymbol{v}^i = \boldsymbol{F}^i \boldsymbol{V}^i, \qquad \boldsymbol{F}^i = \nabla \boldsymbol{\varphi}^i, \qquad \nabla(\cdot) = \frac{\partial(\cdot)}{\partial \boldsymbol{X}^i}, \tag{7}$$

where $\boldsymbol{F}^i$ is the deformation gradient.

The contact traction vector $\boldsymbol{t} = \boldsymbol{t}^2$ is decomposed into normal and tangential components,

$$\boldsymbol{t} = t_N \boldsymbol{n} + \boldsymbol{t}_T, \qquad t_N = \boldsymbol{t} \cdot \boldsymbol{n}, \qquad \boldsymbol{t}_T = t_{T\alpha} \boldsymbol{\tau}^\alpha, \tag{8}$$

where $\boldsymbol{t}^2 = \boldsymbol{\sigma}^2 \boldsymbol{n}$, $\boldsymbol{\sigma}^2$ is the Cauchy stress, and $\boldsymbol{t}^2 = -\boldsymbol{t}^1$ in view of the action-reaction principle. The kinematical contact variables (g_N, $\boldsymbol{v}_T$) and the contact tractions (t_N, $\boldsymbol{t}_T$) are related by the unilateral contact law,

$$g_N \geq 0, \qquad t_N \leq 0, \qquad g_N t_N = 0, \tag{9}$$

and by the Coulomb friction law,

$$\|\boldsymbol{t}_T\| + \mu t_N \leq 0, \qquad \|\boldsymbol{v}_T\| \boldsymbol{t}_T = \boldsymbol{v}_T \|\boldsymbol{t}_T\|, \qquad \|\boldsymbol{v}_T\| (\|\boldsymbol{t}_T\| + \mu t_N) = 0. \tag{10}$$

Finally, the virtual work principle of the two-body system reads [22, 23]

$$\sum_{i=1}^{2} \left(\int_{\Omega^i} \boldsymbol{P}^i \cdot \nabla \delta \boldsymbol{\varphi}^i \mathrm{d}V - \int_{\Gamma_s^i} \boldsymbol{T}^{*i} \cdot \delta \boldsymbol{\varphi}^i \mathrm{d}S \right) + \int_{\Gamma_c^1} (T_N \delta g_N + T_{T\alpha} \delta \bar{\xi}^\alpha) \mathrm{d}S = 0, \tag{11}$$

where $\delta \boldsymbol{\varphi}^i = \boldsymbol{0}$ on Γ_u^i, $\boldsymbol{T}^{*i}$ is the traction prescribed on Γ_s^i, $\boldsymbol{P}^i = \partial \phi^i / \partial \boldsymbol{F}^i$ is the first Piola–Kirchhoff stress, and $\phi^i(\boldsymbol{F}^i)$ is the elastic strain energy

function. The contact contribution in (11) is integrated over the undeformed contact surface Γ_c^1 of the slave body, so the nominal contact tractions T_N and $\boldsymbol{T}_T$,

$$T_N = j^1 t_N, \qquad \boldsymbol{T}_T = j^1 \boldsymbol{t}_T, \tag{12}$$

are introduced, which refer to the unit area in the undeformed configuration Ω^1 of the slave body. Here, $j^i = \mathrm{d}s^i/\mathrm{d}S^i$ is the area transformation factor (which follows from the Nanson's formula, $\boldsymbol{n}\mathrm{d}s = J\boldsymbol{F}^{-T}\boldsymbol{N}\mathrm{d}S$).

Wear rate is a postprocessing quantity that can be computed once the contact problem is solved. According to the classical Archard's wear model, the wear rate is proportional to the product of the normal contact pressure and sliding velocity or, equivalently, proportional to the frictional dissipation rate which is equal to the product of friction stress and sliding velocity. The wear model of the Archard type, consistently formulated in the finite-deformation setting, takes the following form [11],

$$\dot{W}^i = K^i \dot{D}^i, \qquad \dot{D}^i = j^i \dot{d} = j^i \boldsymbol{t}_T \cdot \boldsymbol{v}_T, \tag{13}$$

where K^i is the wear coefficient, and the nominal wear rate $\dot{W}^i$ is the wear volume per unit area and unit time, where both the volume and the area refer to the undeformed configuration Ω^i. The frictional dissipation rate $\dot{d}$ is the dissipated power per unit area in the current configuration ω^i, while $\dot{D}^i$ is referred to the area in the undeformed configuration Ω^i.

2.4. Shape evolution problem

The shape evolution problem is governed by Eq. (2) which defines only the normal component of the shape transformation mapping $\dot{\boldsymbol{\Psi}}^i$ on the boundary $\hat{\Gamma}^i$. It is convenient to uniquely specify also the tangential component of $\dot{\boldsymbol{\Psi}}^i$ by adopting the shape evolution law in the following form

$$\dot{\boldsymbol{\Psi}}^i = \begin{cases} -\dot{W}^i \boldsymbol{N}^i & \text{on } \hat{\Gamma}_c^i, \\ \boldsymbol{0} & \text{on } \hat{\Gamma}^i \setminus \hat{\Gamma}_c^i. \end{cases} \tag{14}$$

In order to arrive at a feasible computational scheme, a suitable time integration of the above time-continuous setting must be introduced, and two first-order integration schemes are discussed below. Two subsequent discrete time instants t_n and $t_{n+1} = t_n + \Delta t$ are thus considered, and a subscript is used to denote the quantities evaluated at a discrete time instant, e.g., $\boldsymbol{\Psi}_n^i(\hat{\boldsymbol{X}}^i) = \boldsymbol{\Psi}^i(\hat{\boldsymbol{X}}^i, t_n)$.

2.4.1. Explicit forward-Euler time integration scheme

Application of the explicit forward-Euler time integration scheme to (14) gives

$$\boldsymbol{\Psi}^i_{n+1}(\hat{\boldsymbol{X}}^i) = \boldsymbol{\Psi}^i_n(\hat{\boldsymbol{X}}^i) - \Delta t\, \dot{W}^i_n(\hat{\boldsymbol{X}}^i)\boldsymbol{N}^i_n(\hat{\boldsymbol{X}}^i) \qquad \text{on } \hat{\Gamma}^i_c, \tag{15}$$

where $\boldsymbol{N}^i_n$ and $\dot{W}^i_n$ depend on the position $\hat{\boldsymbol{X}}^i$ in the initial configuration through the shape transformation mapping $\boldsymbol{\Psi}^i_n$.

Equation (15) can be rewritten as

$$\boldsymbol{X}^i_{n+1} = \boldsymbol{X}^i_n - \Delta t\, \dot{W}^i_n(\boldsymbol{X}^i_n)\boldsymbol{N}^i_n(\boldsymbol{X}^i_n), \tag{16}$$

for $\boldsymbol{X}^i_n \in \Gamma^i_{c,n}$. This form is the basis of a simple and popular shape update scheme employing remeshing after the contact problem is solved at each time step, e.g. [6–10]. In the context of the finite element method, the shape update (16) is applied to the boundary nodes. Subsequently, the positions of the interior nodes are determined in a remeshing procedure.

The above explicit scheme is simple, but it is only *conditionally stable*. As shown by Johansson [5], the critical time increment Δt_{cr} is proportional to the characteristic mesh size h and inversely proportional to the elastic modulus E, so that the time increment must satisfy the stability condition

$$\Delta t < \Delta t_{\text{cr}}, \qquad \Delta t_{\text{cr}} \sim \frac{h}{E}. \tag{17}$$

This is also illustrated in Section 4.1. In realistic conditions, the critical time increment may be very small so that the scheme becomes computationally expensive.

2.4.2. Implicit backward-Euler time integration scheme

Application of the implicit backward-Euler time integration scheme to (14) gives

$$\boldsymbol{\Psi}^i_{n+1}(\hat{\boldsymbol{X}}^i) = \boldsymbol{\Psi}^i_n(\hat{\boldsymbol{X}}^i) - \Delta t\, \dot{W}^i_{n+1}(\hat{\boldsymbol{X}}^i)\boldsymbol{N}^i_{n+1}(\hat{\boldsymbol{X}}^i) \qquad \text{on } \hat{\Gamma}^i_c. \tag{18}$$

In this scheme, the normal $\boldsymbol{N}^i_{n+1}$ and the solution of the deformation problem at t_{n+1}, including the wear rate $\dot{W}^i_{n+1}$, depend on $\boldsymbol{\Psi}^i_{n+1}$. Thus the problem must be solved simultaneously for $\boldsymbol{\varphi}^i_{n+1}$ (displacements) and $\boldsymbol{\Psi}^i_{n+1}$ (shape transformation). Of course, the size of the problem increases due to additional unknowns.

However, the benefit is that the scheme is *unconditionally stable*, so the time increment is limited only by the desired accuracy and not by the stability

condition. In practice, significantly larger time increments can be used as compared to the explicit scheme, thus leading to a computationally efficient scheme.

2.5. Auxiliary elasticity problem

In the shape evolution problem discussed above, the shape transformation mapping is prescribed only on the boundary $\hat{\Gamma}^i$. This uniquely defines the shape changes. In order to define the shape transformation mapping $\boldsymbol{\Psi}^i$ in the whole domain $\hat{\Omega}^i$, we introduce an auxiliary elasticity problem which governs the motion due to shape transformation that is prescribed on the boundary $\hat{\Gamma}^i$.

For that purpose, we introduce an artificial elastic strain energy function $\hat{\phi}^i(\hat{\boldsymbol{F}}^i)$, where the deformation gradient $\hat{\boldsymbol{F}}^i$ is associated with the shape transformation mapping $\boldsymbol{\Psi}^i$,

$$\hat{\boldsymbol{F}}^i = \hat{\nabla}\boldsymbol{\Psi}^i, \qquad \hat{\nabla}(\cdot) = \frac{\partial(\cdot)}{\partial \hat{\boldsymbol{X}}^i}. \tag{19}$$

The auxiliary elastic strain energy function $\hat{\phi}^i(\hat{\boldsymbol{F}}^i)$ can in general be different than the elastic strain energy function $\phi^i(\boldsymbol{F}^i)$ that specifies the actual behaviour of the respective body $\mathcal{B}^i$.

For each body $\mathcal{B}^i$, the shape evolution problem is then governed by the following constrained minimization problem

$$\min_{\boldsymbol{\Psi}^i_{n+1}} \int_{\hat{\Omega}^i} \hat{\phi}^i(\hat{\boldsymbol{F}}^i_{n+1})\,\mathrm{d}\hat{V} \quad \text{subject to } \boldsymbol{\Psi}^i_{n+1} = \boldsymbol{\Psi}^{*i}_{n+1} \text{ on } \hat{\Gamma}^i_c, \tag{20}$$

where $\boldsymbol{\Psi}^i_{n+1} = \boldsymbol{0}$ on $\hat{\Gamma}^i \setminus \hat{\Gamma}^i_c$. The deformation in this auxiliary elasticity problem is driven by the shape transformation $\boldsymbol{\Psi}^{*i}_{n+1}$ that results from wear and is prescribed on the contact boundary $\hat{\Gamma}^i_c$,

$$\boldsymbol{\Psi}^{*i}_{n+1}(\hat{\boldsymbol{X}}^i) = \boldsymbol{\Psi}^i_n(\hat{\boldsymbol{X}}^i) - \Delta t\, \dot{W}^i_{n+\alpha}(\hat{\boldsymbol{X}}^i)\boldsymbol{N}^i_{n+\alpha}(\hat{\boldsymbol{X}}^i). \tag{21}$$

Here, the implicit time integration scheme (18) is obtained by setting $\alpha = 1$, and the explicit time integration scheme (15) is obtained for $\alpha = 0$. This provides a uniform framework for implementation and analysis of both integration schemes.

The shape transformation (21) is introduced in the auxiliary elasticity problem (20) as a constraint rather than as a Dirichlet boundary condition

because $\boldsymbol{\Psi}^{*i}_{n+1}$ is actually an unknown in the complete wear problem. This condition is enforced using Lagrange multipliers $\boldsymbol{\mu}$ and the stationarity of the corresponding Lagrangian $\hat{\mathcal{L}} = \int_{\hat{\Omega}^i} \hat{\phi}^i \mathrm{d}\hat{V} - \int_{\hat{\Gamma}^i_c} \boldsymbol{\mu} \cdot (\boldsymbol{\Psi}^i_{n+1} - \boldsymbol{\Psi}^{*i}_{n+1}) \mathrm{d}\hat{S}$ yields the following variational statement,

$$\int_{\hat{\Omega}^i} \hat{\boldsymbol{P}}^i \cdot \hat{\nabla} \delta\boldsymbol{\Psi}^i \, \mathrm{d}\hat{V} - \int_{\hat{\Gamma}^i_c} [\boldsymbol{\mu} \cdot \delta\boldsymbol{\Psi}^i + \delta\boldsymbol{\mu} \cdot (\boldsymbol{\Psi}^i_{n+1} - \boldsymbol{\Psi}^{*i}_{n+1})] \, \mathrm{d}\hat{S} = 0, \tag{22}$$

where $\hat{\boldsymbol{P}}^i = \partial\hat{\phi}^i / \partial\hat{\boldsymbol{F}}^i$ and $\delta\boldsymbol{\Psi}^i = \boldsymbol{0}$ on $\hat{\Gamma}^i \setminus \hat{\Gamma}^i_c$.

Remark 1. In the present formulation, the shape evolution problem (22) and the deformation problem (11) are coupled, and the two problems are solved simultaneously. This is necessary in the case of the implicit scheme (18) which is the main concern of this work. In the case of the explicit scheme (15), the two problems decouple and could be solved separately in a sequential manner, thus leading to a more efficient implementation.

Remark 2. In order to reduce the computational cost, the shape transformation mapping $\boldsymbol{\Psi}^i$ can be prescribed to identity away from the actual contact zone. This would correspond to solving the auxiliary elasticity problem on a subdomain of $\hat{\Omega}^i$.

3. Finite element implementation

3.1. Preliminaries

The present finite element implementation and the numerical examples reported in Section 4 are restricted to rigid-deformable contact (one body is rigid) and gross sliding (as, for instance, in the pin-on-disc configuration). Below, the specific formulation is detailed, including the augmented Lagrangian treatment of the contact constraints.

In the following, a typical time instant $t = t_{n+1}$ is considered, and it is assumed that the solution at the previous time step $t = t_n$ is known. To simplify the notation, the subscript denoting the quantities evaluated at the current time step t_{n+1} is dropped.

The contact problem is defined by the virtual work principle (11) and the contact conditions (9) and (10). In this work, the augmented Lagrangian method [25, 26] is used to enforce the unilateral contact condition (9). Since gross sliding is assumed, the friction stress is explicitly expressed in terms of the normal contact traction and sliding direction, and no special treatment is

needed. Upon the augmented Lagrangian treatment, the deformation problem is governed by the following augmented virtual work principle,

$$G_{\boldsymbol{\varphi}}(\boldsymbol{\varphi}, \boldsymbol{\Psi}, \lambda_N; \delta\boldsymbol{\varphi}, \delta\lambda_N) = G_{\boldsymbol{\varphi}}^{\text{int}} + G_{\boldsymbol{\varphi}}^{\text{ext}} + G_{\boldsymbol{\varphi}}^{\text{cont}} = 0, \tag{23}$$

where $G_{\boldsymbol{\varphi}}^{\text{int}}$ and $G_{\boldsymbol{\varphi}}^{\text{ext}}$ denote, respectively, the virtual work of internal and external forces,

$$G_{\boldsymbol{\varphi}}^{\text{int}}(\boldsymbol{\varphi}, \boldsymbol{\Psi}; \delta\boldsymbol{\varphi}) = \int_{\Omega} \boldsymbol{P} \cdot \nabla\delta\boldsymbol{\varphi} \, \mathrm{d}V, \quad G_{\boldsymbol{\varphi}}^{\text{ext}}(\boldsymbol{\varphi}, \boldsymbol{\Psi}; \delta\boldsymbol{\varphi}) = -\int_{\Gamma_s} \boldsymbol{T}^* \cdot \delta\boldsymbol{\varphi} \, \mathrm{d}S. \tag{24}$$

The contact contribution to the virtual work involves an additional field of Lagrange multipliers λ_N defined on the contact surface Γ_c,

$$G_{\boldsymbol{\varphi}}^{\text{cont}}(\boldsymbol{\varphi}, \boldsymbol{\Psi}, \lambda_N; \delta\boldsymbol{\varphi}, \delta\lambda_N) = \int_{\Gamma_c} (\hat{\lambda}_N^{\text{eff}} \delta g_N + \boldsymbol{T}_T \cdot \delta\boldsymbol{g}_T + C_N \delta\lambda_N) \, \mathrm{d}S, \tag{25}$$

where

$$\hat{\lambda}_N^{\text{eff}} = \begin{cases} \hat{\lambda}_N, & \hat{\lambda}_N \leq 0, \\ 0, & \hat{\lambda}_N > 0, \end{cases} \qquad C_N = \begin{cases} g_N, & \hat{\lambda}_N \leq 0, \\ -\lambda_N/\varrho, & \hat{\lambda}_N > 0, \end{cases} \tag{26}$$

$\hat{\lambda}_N = \lambda_N + \varrho g_N$ is the augmented Lagrange multiplier and $\varrho > 0$ is a regularization parameter. Note that C_N is a state-dependent constraint enforcing either $g_N = 0$ in the case of contact or $\lambda_N = 0$ in the case of separation, in agreement with the unilateral contact condition (9). In view of the gross-sliding condition, the friction stress is given by $\boldsymbol{T}_T = -\mu\hat{\lambda}_N^{\text{eff}} \boldsymbol{v}_T / \|\boldsymbol{v}_T\|$. Finally, in the case of rigid-deformable contact, the variations of the kinematical quantities are simply given by $\delta g_N = \boldsymbol{n} \cdot \delta\boldsymbol{x}$ and $\delta\boldsymbol{g}_T = (\boldsymbol{1} - \boldsymbol{n} \otimes \boldsymbol{n})\delta\boldsymbol{x}$.

The shape evolution problem (22) is rewritten in the form

$$G_{\boldsymbol{\Psi}}(\boldsymbol{\varphi}, \boldsymbol{\Psi}, \lambda_N, \boldsymbol{\mu}; \delta\boldsymbol{\Psi}, \delta\boldsymbol{\mu}) = G_{\boldsymbol{\Psi}}^{\text{int}} + G_{\boldsymbol{\Psi}}^{\text{cont}} = 0, \tag{27}$$

where

$$G_{\boldsymbol{\Psi}}^{\text{int}}(\boldsymbol{\Psi}; \delta\boldsymbol{\Psi}) = \int_{\hat{\Omega}} \hat{\boldsymbol{P}} \cdot \hat{\nabla}\delta\boldsymbol{\Psi} \, \mathrm{d}\hat{V} \tag{28}$$

and

$$G_{\boldsymbol{\Psi}}^{\text{cont}}(\boldsymbol{\varphi}, \boldsymbol{\Psi}, \lambda_N, \boldsymbol{\mu}; \delta\boldsymbol{\Psi}, \delta\boldsymbol{\mu}) = -\int_{\hat{\Gamma}_c} [\hat{\boldsymbol{\mu}} \cdot \delta\boldsymbol{\Psi} + \delta\boldsymbol{\mu} \cdot (\boldsymbol{\Psi} - \boldsymbol{\Psi}^*)] \, \mathrm{d}\hat{S}. \tag{29}$$

In the present implementation, the constraint $\boldsymbol{\Psi} = \boldsymbol{\Psi}^*$ has been actually enforced using the augmented Lagrangian method, hence the augmented Lagrange multiplier $\hat{\boldsymbol{\mu}} = \boldsymbol{\mu} + \epsilon(\boldsymbol{\Psi} - \boldsymbol{\Psi}^*)$ in Eq. (29) rather than the Lagrange multiplier $\boldsymbol{\mu}$ alone as in Eq. (22). This treatment proved to have beneficial effect on the convergence of the Newton method used to solve the nonlinear finite element equations.

The deformation problem depends on the current shape of the undeformed configuration Ω and this is indicated by the dependence of $G_{\boldsymbol{\varphi}}$ on the shape transformation mapping $\boldsymbol{\Psi}$ in Eqs. (23)–(25). The dependence of $G^{\text{cont}}_{\boldsymbol{\Psi}}$ on the deformation mapping $\boldsymbol{\varphi}$ and on the Lagrange multiplier λ_N is through the term $\boldsymbol{\Psi}^*$, and specifically through the wear rate $\dot{W}$ in Eq. (21).

The finite element implementation has been carried out using the *AceGen/AceFEM* system [27, 28]. Implementation heavily relies on the automation capabilities of the *AceGen* system, in particular on the automatic differentiation (AD) technique implemented in *AceGen*. More details concerning the *AceGen* system, automatic differentiation, and automation of finite element computations can be found in [28] and, in the context of contact problems, in [29].

The AD-based formulation of the solid and contact elements used in this work is provided below. Note that this compact formulation is sufficient for the actual implementation, as the specific formulae and the corresponding computer codes are generated automatically by the *AceGen* system.

3.2. Solid elements

Solid elements implement the internal-work contributions $G^{\text{int}}_{\boldsymbol{\varphi}}$ and $G^{\text{int}}_{\boldsymbol{\Psi}}$ in the weak forms (23) and (27), respectively. Application of the standard finite element interpolation and numerical integration gives the global residual vector $\mathbf{R}^{\text{int}}$ associated with the global vector of nodal unknowns $\mathbf{p}$,

$$G^{\text{int}} = G^{\text{int}}_{\boldsymbol{\varphi}} + G^{\text{int}}_{\boldsymbol{\Psi}} = \delta\mathbf{p} \cdot \mathbf{R}^{\text{int}}. \tag{30}$$

The global residual $\mathbf{R}^{\text{int}}$ is an assembly of element residuals $\mathbf{R}_e$, and each element residual is a sum of Gauss-point contributions $\mathbf{R}_g$,

$$\mathbf{R}^{\text{int}} = \mathop{\mathsf{A}}_{e \in \mathcal{S}_s} \mathbf{R}_e, \qquad \mathbf{R}_e = \textstyle\sum_g w_g \mathbf{R}_g, \tag{31}$$

where $\mathcal{S}_s$ is the set of solid elements, and w_g denotes the Gauss-point weight.

The element unknowns $\mathbf{p}_e$ comprise the nodal displacements $\mathbf{p}^e_{\boldsymbol{\varphi}}$ related to the deformation mapping $\boldsymbol{\varphi}$ and displacement-like quantities $\mathbf{p}^e_{\boldsymbol{\Psi}}$ related

to the shape transformation mapping $\boldsymbol{\Psi}$, thus $\mathbf{p}_e = \{\mathbf{p}^e_{\boldsymbol{\varphi}}, \mathbf{p}^e_{\boldsymbol{\Psi}}\}$. The Gauss-point residual $\mathbf{R}_g$ is obtained by applying the automatic differentiation (AD) technique according to

$$\mathbf{R}_g = J_g \left.\frac{\delta\phi}{\delta\mathbf{p}_e}\right|_{\frac{\mathrm{D}\phi}{\mathrm{D}\mathbf{p}^e_{\boldsymbol{\Psi}}}=\mathbf{0}} + \hat{J}_g \frac{\delta\hat{\phi}}{\delta\mathbf{p}_e}, \tag{32}$$

where $J_g = \det(\partial\boldsymbol{X}/\partial\boldsymbol{\xi})$ is the Jacobian of the transformation from the reference element $\Omega_\square$ to the undeformed configuration Ω, and similarly $\hat{J}_g = \det(\partial\hat{\boldsymbol{X}}/\partial\boldsymbol{\xi})$ is the Jacobian relating $\Omega_\square$ and the initial configuration $\hat{\Omega}$. The operator $\delta(\cdot)/\delta(\cdot)$ denotes the differentiation performed by the AD algorithm, cf. [28]. The undeformed configuration Ω should not be perturbed when evaluating the virtual work contribution $G^{\mathrm{int}}_{\boldsymbol{\varphi}}$, cf. Eq. $(24)_1$, and this is enforced by introducing the AD exception in the first term on the right-hand side in Eq. (32). It is easy to check that the above AD-based formulation indeed corresponds to the internal-work contributions (24) and (28), see also [28].

In the present implementation, the F-bar formulation [30] is employed to avoid volumetric locking effects that may occur in case of nearly incompressible materials: a 4-node quadrilateral F-bar element is used in 2D problems and an 8-node hexahedral F-bar element is used in 3D problems. The auxiliary elasticity problem is discretized using bilinear (2D) or trilinear (3D) isoparametric elements.

3.3. Contact elements

The contact surface $\hat{\Gamma}_c$ is discretized into 2-node linear segments in 2D and 4-node bilinear facets in 3D. The same interpolation is used for the Lagrange multipliers λ_N and $\boldsymbol{\mu}$. Nodal integration is used in order to avoid spurious oscillations typical for Gauss quadrature [31]. Upon discretization, the contact contribution can be expressed in terms of the global residual vector $\mathbf{R}^{\mathrm{cont}}$,

$$G^{\mathrm{cont}} = G^{\mathrm{cont}}_{\boldsymbol{\varphi}} + G^{\mathrm{cont}}_{\boldsymbol{\Psi}} = \delta\mathbf{p}\cdot\mathbf{R}^{\mathrm{cont}}. \tag{33}$$

As in the case of solid elements, we have

$$\mathbf{R}^{\mathrm{cont}} = \mathop{\mathsf{A}}_{e\in\mathcal{S}_c} \mathbf{R}_e, \qquad \mathbf{R}_e = \textstyle\sum_g w_g \mathbf{R}_g, \tag{34}$$

where $\mathcal{S}_c$ is the set of contact elements.

In addition to the nodal displacements $\mathbf{p}^e_{\boldsymbol{\varphi}}$ and displacement-like quantities $\mathbf{p}^e_{\boldsymbol{\Psi}}$, the element unknowns $\mathbf{p}_e$ comprise now the contact Lagrange multipliers assembled in $\mathbf{p}^e_\lambda$ and the Lagrange multipliers that enforce the shape transformation, which are assembled in $\mathbf{p}^e_{\boldsymbol{\mu}}$, thus $\mathbf{p}_e = \{\mathbf{p}^e_{\boldsymbol{\varphi}}, \mathbf{p}^e_{\boldsymbol{\Psi}}, \mathbf{p}^e_\lambda, \mathbf{p}^e_{\boldsymbol{\mu}}\}$. The Gauss-point residual $\mathbf{R}_g$ corresponding to the contact contribution specified by Eqs. (25) and (29) is obtained using the following formulation

$$\begin{aligned}\mathbf{R}_g \;=\; j_g \left[(\hat{\lambda}_N^{\text{eff}} \boldsymbol{n} + \boldsymbol{T}_T) \cdot \frac{\delta \boldsymbol{x}}{\delta \mathbf{p}_e}\bigg|_{\frac{\mathrm{D}\boldsymbol{x}}{\mathrm{D}\mathbf{p}^e_{\boldsymbol{\Psi}}}=\mathbf{0}} + C_N \frac{\delta \lambda_N}{\delta \mathbf{p}_e} \right] \\ + \hat{j}_g \left[\hat{\boldsymbol{\mu}} \cdot \frac{\delta \boldsymbol{\Psi}}{\delta \mathbf{p}_e} + (\boldsymbol{\Psi} - \boldsymbol{\Psi}^*) \cdot \frac{\delta \boldsymbol{\mu}}{\delta \mathbf{p}_e} \right], \end{aligned} \tag{35}$$

where $j_g = \|\partial \boldsymbol{X}/\partial\xi \times \partial \boldsymbol{X}/\partial\eta\|$ and $\hat{j}_g = \|\partial \hat{\boldsymbol{X}}/\partial\xi \times \partial \hat{\boldsymbol{X}}/\partial\eta\|$ is the Jacobian of the parametrization of the element, respectively, in the undeformed configuration Ω and in the initial configuration $\hat{\Omega}$. More details on automation of contact formulations can be found in [29].

3.4. Monolithic solution scheme and linearization

The nonlinear equations $\mathbf{R}(\mathbf{p}) = \mathbf{0}$ are solved simultaneously for all unknowns $\mathbf{p} = \{\mathbf{p}_{\boldsymbol{\varphi}}, \mathbf{p}_{\boldsymbol{\Psi}}, \mathbf{p}_\lambda, \mathbf{p}_{\boldsymbol{\mu}}\}$ using the Newton's method. The global residual vector $\mathbf{R} = \mathbf{R}^{\text{int}} + \mathbf{R}^{\text{ext}} + \mathbf{R}^{\text{cont}}$ results from the finite element discretization: $\mathbf{R}^{\text{int}}$ and $\mathbf{R}^{\text{cont}}$ have been introduced above; the external-work residual $\mathbf{R}^{\text{ext}}$ corresponding to $G^{\text{ext}}_{\boldsymbol{\varphi}}$ is obtained trivially, particularly for conservative loading (the details are omitted here). At each Newton iteration, the following linear problem is solved for $\Delta\mathbf{p}^{(i)}$,

$$\mathbf{K}^{(i)} \Delta \mathbf{p}^{(i)} + \mathbf{R}^{(i)} = \mathbf{0}, \tag{36}$$

where $\mathbf{R}^{(i)}$ and $\mathbf{K}^{(i)}$ are evaluated at $\mathbf{p}^{(i)}$, and the approximate solution is updated, $\mathbf{p}^{(i+1)} = \mathbf{p}^{(i)} + \Delta\mathbf{p}^{(i)}$, until convergence is obtained. The tangent matrix $\mathbf{K}^{(i)}$ is an assembly of element tangent matrices $\mathbf{K}^{(i)}_e$,

$$\mathbf{K}^{(i)} = \mathop{\mathsf{A}}_{e \in \mathcal{S}_s \cup \mathcal{S}_c} \mathbf{K}^{(i)}_e, \qquad \mathbf{K}^{(i)}_e = \frac{\delta \mathbf{R}^{(i)}_e}{\delta \mathbf{p}_e}, \tag{37}$$

which are obtained using automatic differentiation. Thanks to exact linearization, quadratic convergence of the Newton scheme is achieved.

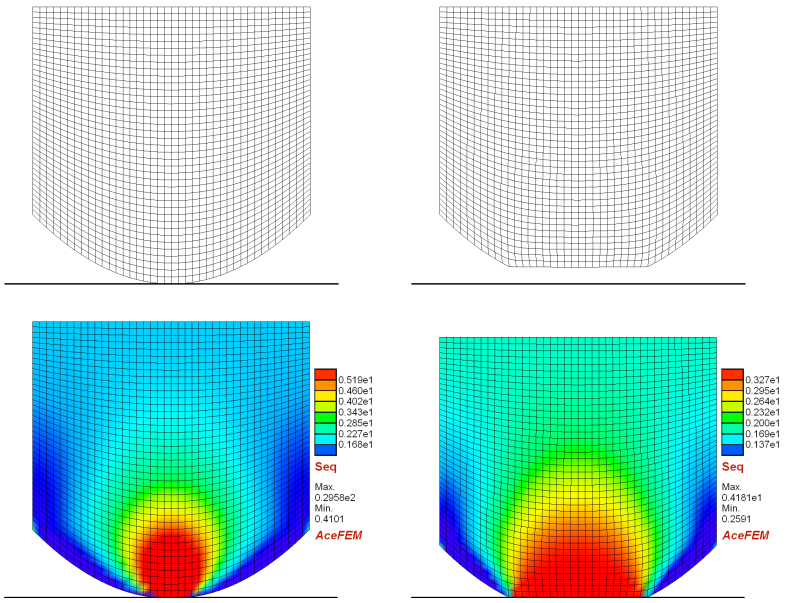

(a) (b)

Figure 1: Two-dimensional pin-on-flat problem, small-deformation regime ($E = 640$ MPa). Finite element mesh in the undeformed configuration (top) and equivalent stress σ_{eq} in the deformed configuration (bottom): (a) at the initial time instant $t = 0$ and (b) at the final time instant $t = 1000$ s.

4. Numerical examples

4.1. Two-dimensional pin-on-flat problem

The purpose of the first example is to study quantitatively the stability and accuracy of the two time integration schemes introduced in Section 2.4. A two-dimensional frictionless contact and wear problem in plane-strain conditions is considered. A hyperelastic pin is pressed into a rigid plane which is moving laterally with velocity $v = 1000$ mm/s. The geometry and the mesh of 40×40 elements are shown in Fig. 1a. The contact surface at the bottom of the pin is a parabola $y = x^2/(2R)$ with the radius of curvature in the centre $R = 5$ mm. The maximum height of the pin is $H = 10$ mm and its width is $L = 10$ mm. The lateral boundaries are constrained in the lateral direction and free to move in the vertical direction. A uniform traction is applied at the top of the pin, the total force is $F = 20$ N/mm.

Since frictionless contact is considered in this example, the wear rate is assumed to be proportional to the product of normal contact pressure and

sliding velocity, $\dot{W} = kv|T_N|$, and the wear coefficient is $k = 10^{-7}$ MPa^{-1}. The duration of the simulated wear process is $t_{\max} = 1000$ s.

The hyperelastic material model is of the neo-Hookean type. The elastic strain energy is adopted in the following form

$$\phi(\boldsymbol{F}) = \frac{1}{2}\lambda(J-1)^2 + \mu\left(\frac{1}{2}(\operatorname{tr}\boldsymbol{C} - 3) - \log J\right), \tag{38}$$

where $\boldsymbol{C} = \boldsymbol{F}^{\mathrm{T}}\boldsymbol{F}$, $J = \det\boldsymbol{F}$, and λ and μ are the Lamé's parameters that are specified by prescribing the Young's modulus E and Poisson's ratio ν according to $\mu = E/(2(1+\nu))$, $\lambda = 2\mu\nu/(1-2\nu)$. The Poisson's ratio is fixed at $\nu = 0.3$ while the Young's modulus is varied between $E = 10$ MPa and $E = 640$ MPa.

The initial Hertzian pressure corresponding to $E = 640$ MPa is $p_0 = 30$ MPa, so that the ratio $p_0/E = 0.047$ is higher than in typical elastic contacts. However, considering that the pressure significantly decreases during the wear process (as the contact area increases), the case of $E = 640$ MPa will be referred to as the *small-deformation regime*.[1] Figure 1 shows the undeformed configuration and the deformed configuration at the initial and final time instants. Evolution of the shape of the contact surface is presented in Fig. 2. It is seen that the time increment $\Delta t = 200$ s is higher than the critical one for the explicit scheme, and the corresponding results exhibit numerical instability, see Fig. 2b. The instability of the explicit scheme does not occur for a smaller time increment of $\Delta t = 5$. From Fig. 2a it is seen that the implicit scheme is capable of accurately reproducing significant configuration changes in just 5 time steps.

The *finite-deformation regime* corresponds to the lower values of the elastic modulus E. Indeed, finite deformations are clearly visible in Fig. 3 which shows the solution obtained for $E = 20$ MPa. Shape evolution is presented in Fig. 4, and it is seen that instability of the explicit scheme does not occur even for the large time increment of $\Delta t = 200$ s, and both integration schemes produce similar results.

The effect of the elastic modulus E, mesh density and time increment Δt on the accuracy of the solution is illustrated in Figs. 5 and 6. The time increment Δt has been varied between 1.56 s and 200 s. The solution

[1]Note that, in order to reduce the ratio p_0/E to the value of 0.012 (which is still rather high), the elastic modulus would have to be increased 16 times (to $E = 10.2$ GPa).

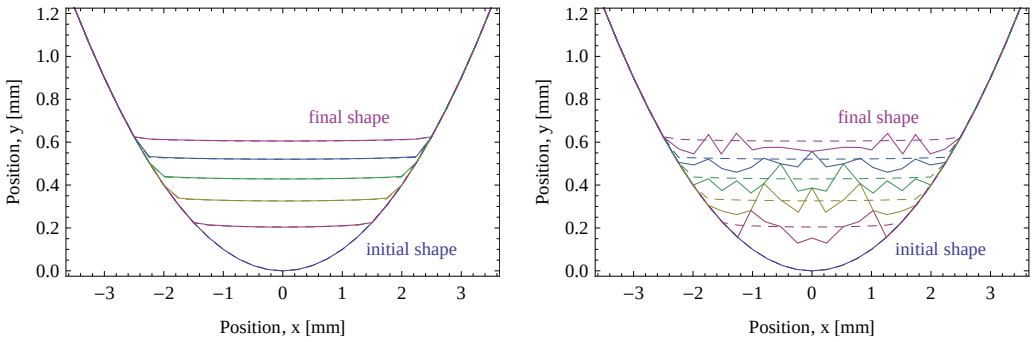

Figure 2: Two-dimensional pin-on-flat problem, small-deformation regime ($E = 640$ MPa). Shape evolution obtained in 5 time steps ($\Delta t = 200$ s, solid lines) and in 200 time steps ($\Delta t = 5$ s, dashed lines) using (a) the implicit and (b) the explicit time integration scheme.

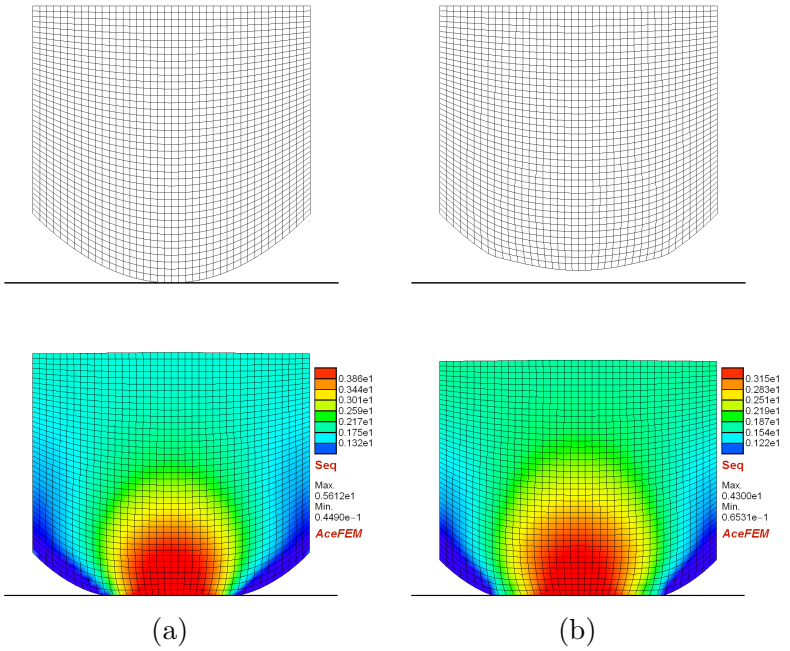

Figure 3: Two-dimensional pin-on-flat problem, finite-deformation regime ($E = 20$ MPa). Finite element mesh in the undeformed configuration (top) and equivalent stress σ_{eq} in the deformed configuration (bottom): (a) at the initial time instant $t = 0$ and (b) at the final time instant $t = 1000$ s.

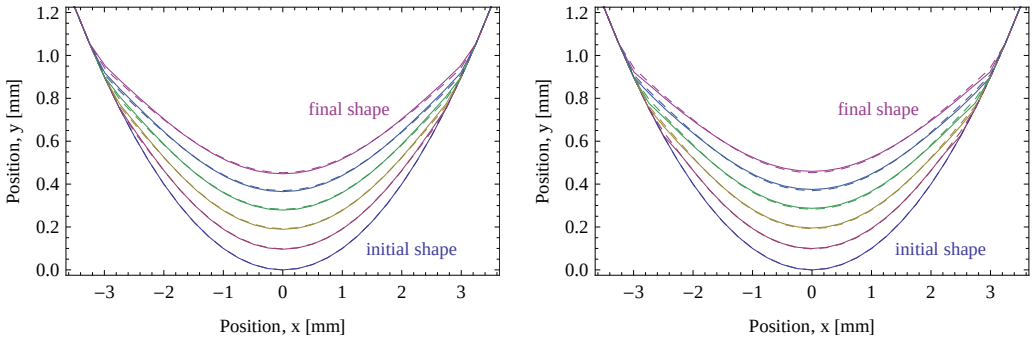

Figure 4: Two-dimensional pin-on-flat problem, finite-deformation regime ($E = 20$ MPa). Shape evolution obtained in 5 time steps ($\Delta t = 200$ s, solid lines) and in 200 time steps ($\Delta t = 5$ s, dashed lines) using (a) the implicit and (b) the explicit time integration scheme.

is completed in 640 time steps for $\Delta t = 1.56$ s and in 5 time steps for $\Delta t = 200$ s. The solution error is computed with respect to the reference solution obtained for $\Delta t = 0.78$ s (1280 steps), and the Euclidean norm of the difference of the nodal positions at the contact surface in the final undeformed configuration is taken as the measure of the error.

In the case of the implicit scheme, the solution error increases with increasing time increment in an approximately linear manner. This is expected because the Euler scheme is first-order accurate. Similar behaviour is observed for the explicit scheme at relatively small time increments. However, a sudden increase of the error is observed at larger time increments. This is related to the instability of the explicit forward-Euler scheme. In agreement with the theoretical result of Johansson [5], see also Eq. 17, the critical time increment is proportional to the element size and inversely proportional to the elastic modulus.

4.2. Elastic ball–rigid flat problem

This example is a three-dimensional counterpart of the one studied in the previous subsection. The aim is to demonstrate the feasibility of the proposed approach for realistic three-dimensional contact and wear problems. A hyperelastic ball of radius $R = 5$ mm is pressed into a rigid plane which is moving with velocity $v = 1000$ mm/s. Frictional contact with friction coefficient $\mu = 0.5$ is considered. The duration of the simulated wear process is $t_{\max} = 1000$ s, which is solved in 10 time steps with $\Delta t = 0.1 t_{\max}$.

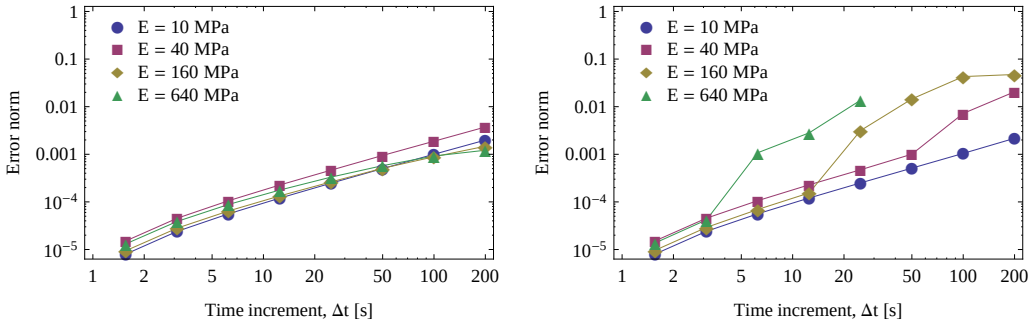

Figure 5: Two-dimensional pin-on-flat problem. Solution error as function of time increment Δt and elastic modulus E for (a) the implicit and (b) the explicit time integration scheme (80×80 elements).

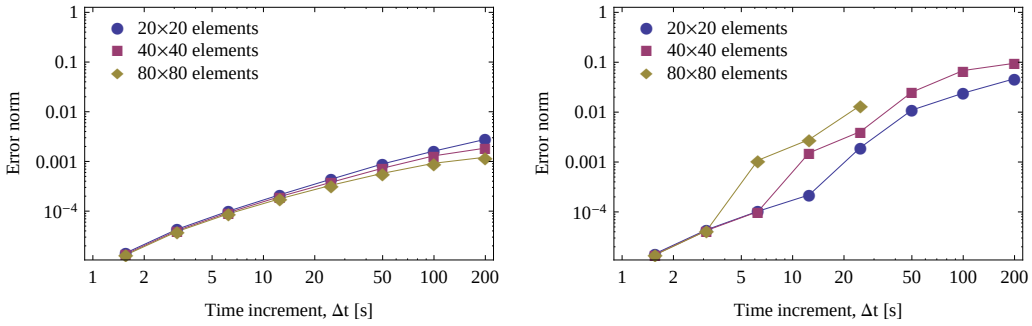

Figure 6: Two-dimensional pin-on-flat problem. Solution error as function of time increment Δt and mesh density for (a) the implicit and (b) the explicit time integration scheme ($E = 640$ MPa).

Two cases are considered. In the *small-deformation regime*, the elastic properties are specified by $E = 100$ GPa and $\nu = 0.3$, the normal force is $F = 100$ N, and the wear coefficient in the Archard model (13) is $K = 10^{-7}$ MPa^{-1}. Considering that the counter-body is rigid, the reduced elastic stiffness of the contact pair is approximately equal to that of two elastic bodies made of steel. The Hertzian pressure is $p_0 = 2.1$ GPa, and the Hertzian contact radius is $a = 0.15$ mm.

In the *finite-deformation regime*, the elastic parameters are $E = 10$ MPa and $\nu = 0.45$, the normal force is $F = 25$ N, and the wear coefficient is $K = 4 \cdot 10^{-7}$ MPa^{-1} (the Hertzian pressure would be now $p_0 = 3.1$ MPa). The adopted parameters are such that the total wear volume at the end of the process is identical in both cases and equal to 5 mm^3.

Loading is applied at the mid-plane of the ball. The tangential displacements are prescribed to be equal to zero, and a uniform normal displacement is enforced using Lagrange multipliers under the condition that the total normal force is equal to the prescribed force. The actual problem involves thus one half of the ball fully constrained at the mid-plane. Considering the symmetry with respect to a plane parallel to the sliding direction, only one quarter of the ball is analyzed. The finite element mesh of 16384 hexahedral elements and 18021 nodes is shown in Fig. 7. The total number of unknowns is 88421 including the displacements, displacement-like quantities describing shape changes, and Lagrange multipliers enforcing contact conditions, shape evolution at the contact interface, and uniform normal displacement at the mid-plane. The total number of unknowns is reduced from 107245 to 88421 by constraining the shape transformation far from the actual contact zone, cf. Remark 2.

Evolution of the shape of the ball in the small-deformation regime is shown in Fig. 7. As the elastic strains are small, the undeformed and deformed configurations are nearly identical. The contact pressure at three time instants is shown in Fig. 8. The initial pressure at $t = 0$ is not included in Fig. 8 because the finite element mesh is too coarse to reasonably reproduce the Hertzian pressure distribution (the element size in the contact area is 0.125 mm, while the Hertzian contact radius is $a = 0.15$ mm). It is seen that the pressure is uniform, and its value decreases with increasing contact area. This response is easily explained by observing that wear causes a rigid-body motion of the ball in the normal direction. The rigid-body motion is then associated with a uniform wear rate which, through the wear model, induces a uniform contact pressure, see [2].

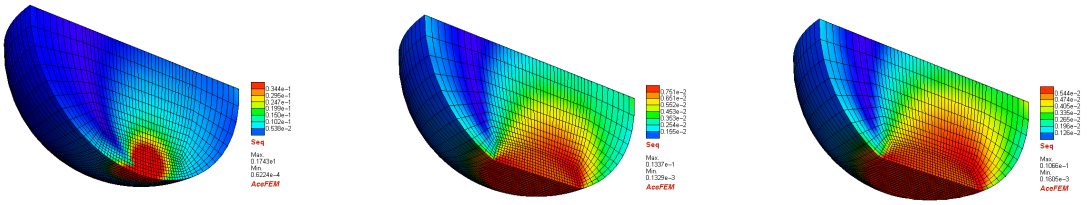

(a) (b) (c)

Figure 7: Elastic ball-rigid flat problem, small-deformation regime. Equivalent stress σ_{eq} in the deformed configuration (the undeformed configuration is nearly identical) at (a) $t = 0$, (b) $t = 500$ s, (c) $= 1000$ s.

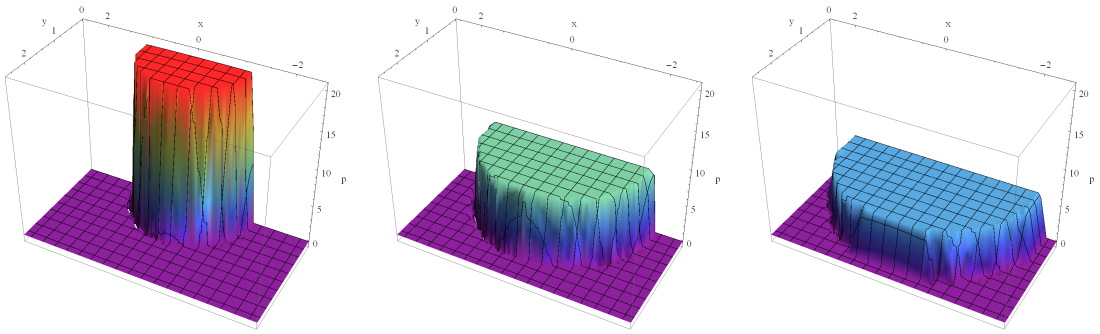

(a) (b) (c)

Figure 8: Elastic ball-rigid flat problem, small-deformation regime. Contact pressure (in MPa) at (a) $t = 100$ s, (b) $t = 500$ s, (c) $t = 1000$ s.

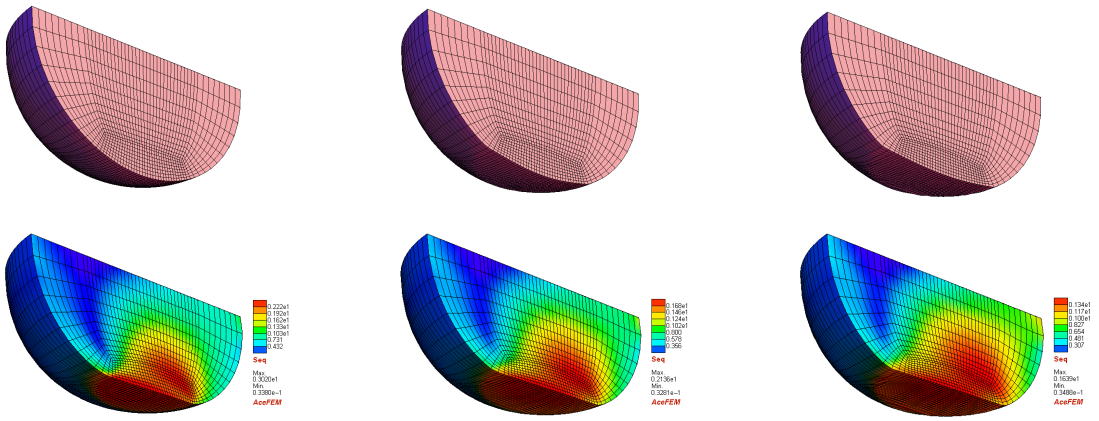

(a) (b) (c)

Figure 9: Elastic ball-rigid flat problem, finite-deformation regime. Undeformed configuration (top) and equivalent stress σ_{eq} in the deformed configuration (bottom) at (a) $t = 0$, (b) $t = 500$ s, (c) $t = 1000$ s.

The critical time increment of the explicit time integration scheme has been estimated to be approximately equal to $\Delta t_{\text{cr}} \approx 0.1$ s. Accordingly, the explicit scheme would require about 10000 time steps to complete the solution. Using the implicit scheme, the solution has been obtained in 17 time steps (at the beginning of the process, the fixed time increment $\Delta t = 100$ s was too large to obtain convergence so that sub-stepping was needed). The gain in computational cost is thus significant (about two orders of magnitude) even considering that the computational cost of one time increment in the implicit scheme is higher than that of the explicit scheme due to increased number of global unknowns.

Figure 9 presents the shape evolution in the finite-deformation regime. Finite changes of both the undeformed and the deformed configuration are clearly visible. The corresponding evolution of contact pressure is shown in Fig. 10. The pressure distribution is not symmetric with respect to the $x = 0$ plane due to friction ($\mu = 0.5$). The effect of friction is also visible in Fig. 9.

The present wear evolution problem has been successfully solved in 10 equal time steps of the implicit time integration scheme (i.e., substepping was not needed). The accuracy of the solution is satisfactory despite the significant changes of the shape. This is illustrated in Fig. 11a in which the pressure profile is compared to the one obtained in 100 time increments. It

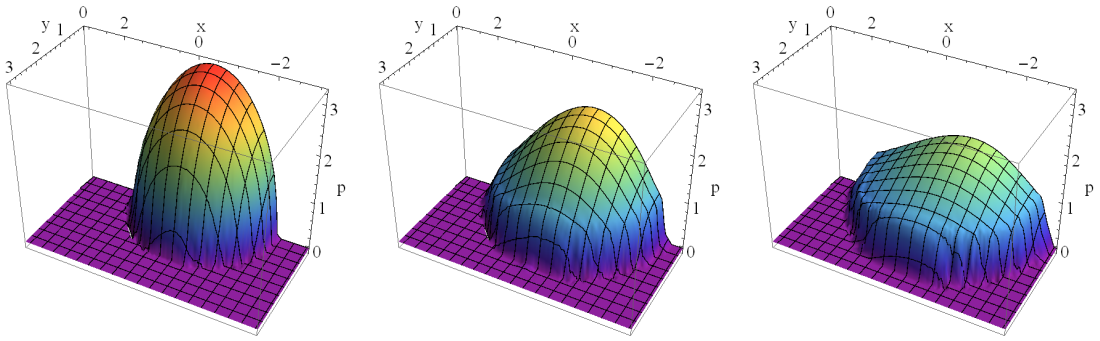

Figure 10: Elastic ball-rigid flat problem, finite-deformation regime. Contact pressure (in MPa) at (a) $t = 0$, (b) $t = 500$ s, (c) $t = 1000$ s.

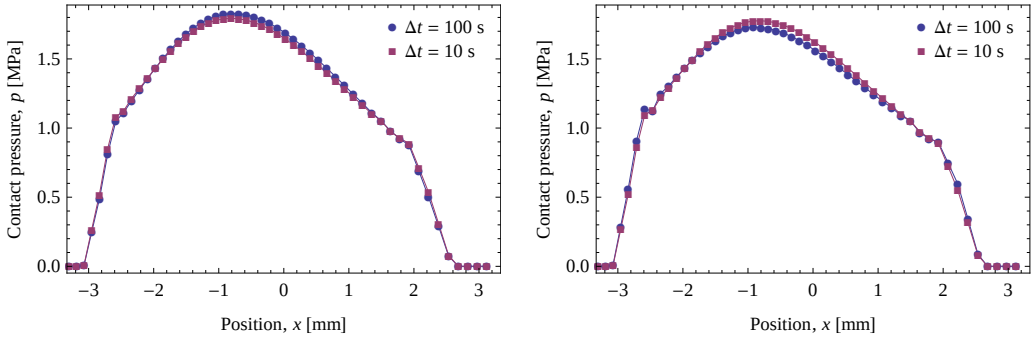

Figure 11: Elastic ball-rigid flat problem, finite-deformation regime. Profile of contact pressure at $y = 0$ obtained using: (a) implicit scheme, (b) explicit scheme.

is seen that the two solutions agree well (the maximum relative difference is below 3%). Figure 11b presents a similar comparison for the explicit scheme. Here, the pressure increases with decreasing time increment, while an opposite effect is observed for the implicit scheme.

The instability of the explicit scheme is not a major issue in the present example for $\Delta t = 100$ s. Nevertheless, the results obtained using the explicit scheme with $\Delta t = 100$ s exhibit moderate oscillations of contact pressure at the edge of the contact zone. This can be seen in Fig. 11b. It has been checked that the explicit scheme becomes unstable when the elastic modulus E is increased from 10 to 20 MPa (while keeping $\Delta t = 100$ s). In view of the results presented in Section 4.1, this suggests that, for $E = 10$ MPa, the

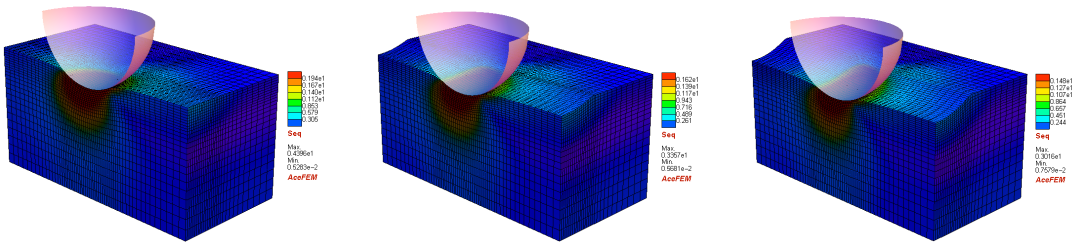

(a) (b) (c)

Figure 12: Rigid ball–elastic half-space problem, finite-deformation regime. Equivalent stress σ_{eq} in the deformed configuration at (a) $t = 0$, (b) $t = 500$ s, (c) $t = 1000$ s.

critical time increment Δt_{cr} is close to 100 s.

4.3. Periodic contact of rigid ball and elastic half-space

In this last example, periodic sliding contact of a rigid ball with a hyperelastic half-space is considered. The coordinate system is attached to the ball so that the half-space is analyzed in an Eulerian frame. Specifically, as discussed in Section 2.3, the Eulerian description of the rigid-body motion in the undeformed configuration is adopted, while the deformation due to contact interaction is treated in the Lagrangian manner. The set-up corresponding to the finite-deformation regime (specified in detail below) is shown in Fig. 12. Due to symmetry, only one half of the block representing the half-space is analyzed.

As the problem is assumed to be a quasi-steady-state wear problem, cf. Section 2.2, the wear groove is uniform along the sliding direction. Accordingly, the shape transformation mapping $\boldsymbol{\Psi}$ is also uniform along the sliding direction, and it is sufficient to prescribe it as a two-dimensional field at one cross-section only. The number of corresponding degrees of freedom in a finite element model is thus a small fraction of the total number of degrees of freedom, and the additional computational cost of solving the coupled deformation and shape evolution problem, as referred to the cost of the deformation problem alone, is small.

The problem under consideration can be treated as a model of the pin-on-disc tribological test in which the curvature of the sliding path is neglected. Wear of the disc is due to repeated contact at each revolution of the disc. Hence, the wear rate governing the evolution of the wear groove must be averaged along the sliding path, and the corresponding parameter L, the

sliding length per cycle, must be specified. In the case of the pin-on-disc test, L is the circumference of the circular sliding path. This parameter is independent from the actual dimensions of the computational domain that is restricted to the neighbourhood of the contact zone in order to reduce the computational cost.

The material and process parameters are the following. The elastic moduli are equal to those adopted in Section 4.2, i.e., $E = 100$ GPa and $\nu = 0.3$ in the small-deformation regime, and $E = 10$ MPa and $\nu = 0.45$ in the finite-deformation regime. The ball radius is $R = 5$ mm, the sliding velocity is $v = 1000$ mm/s, the friction coefficient is $\mu = 0.5$, and the duration of the simulated wear process is $t_{\max} = 1000$ s. In the small-deformation regime, the normal force is $F = 100$ N, the sliding length per cycle is $L = 70$ mm, and the wear coefficient is $K = 4 \cdot 10^{-7}$ MPa^{-1}. In the finite-deformation regime, the corresponding parameters are: $F = 50$ N, $L = 100$ mm, and $K = 2 \cdot 10^{-7}$ MPa^{-1}.

The deformation in the contact zone and the evolution of the wear groove in the finite-deformation regime are shown in Fig. 12, and the corresponding evolution of contact pressure is shown in Fig. 13. The finite element mesh consists of 43200 hexahedral elements and 47275 nodes, and the total number of unknowns is 142508 of which only about 1500 are the displacement-like quantities corresponding to the shape transformation mapping $\mathbf{\Psi}$. The wear evolution problem has been solved with a nominal time increment $\Delta t = 50$ s; however, substepping was needed at the initial stage due to convergence problems so that 32 time steps were needed to complete the solution.

The solution obtained in the small-deformation regime is presented in Figs. 14 and 15. The contact zone is initially circular, which corresponds to the Hertzian contact, and it is elongated once the wear groove forms. The computational domain has been adjusted accordingly so that the evolution of contact conditions can be accurately followed. The length of the elastic block along the sliding direction is 1.4 mm and its half-width is 2 mm, cf. Fig. 14a. The finite element mesh consists of 65600 hexahedral elements and 71463 nodes, and the total number of unknowns is 219432 of which about 3400 are the displacement-like quantities corresponding to the shape transformation mapping $\mathbf{\Psi}$. The initial Hertzian pressure is $p_0 = 2.1$ GPa and the contact radius is $a = 0.15$ mm, and both features are accurately represented by the present finite element solution (element size in the contact zone is 0.015 mm). The nominal time increment was $\Delta t = 50$ s. As in the previous examples, substepping was needed at the initial stage, and the solution was completed

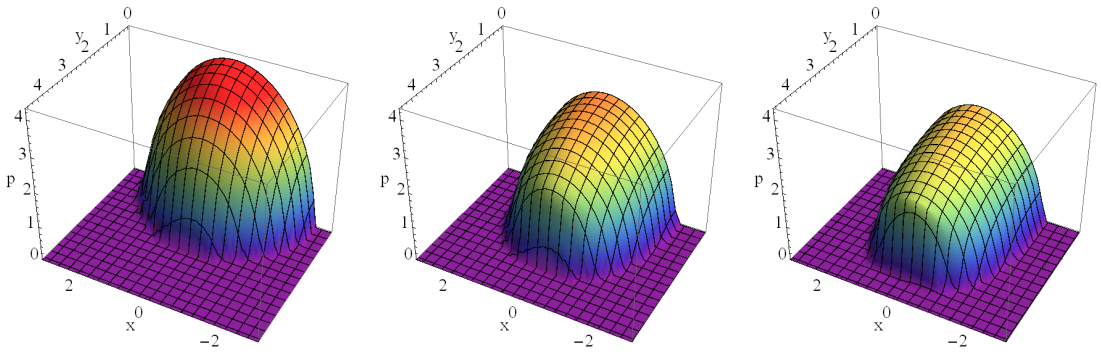

Figure 13: Rigid ball–elastic half-space problem, finite-deformation regime. Contact pressure at (a) $t = 0$, (b) $t = 500$ s, (c) $t = 1000$ s.

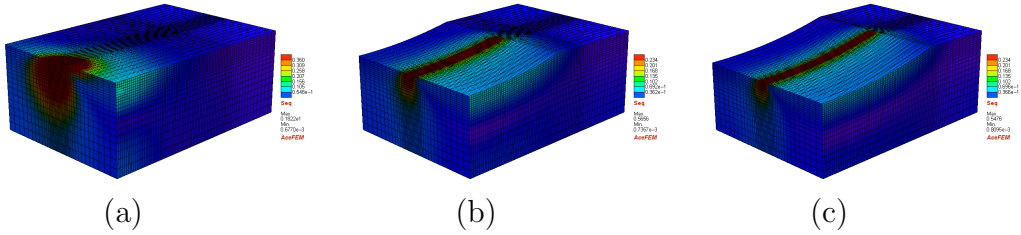

Figure 14: Rigid ball–elastic half-space problem, small-deformation regime. Equivalent stress σ_{eq} in the deformed configuration at (a) $t = 0$, (b) $t = 500$ s, (c) $t = 1000$ s.

in 26 time steps.

Figure 15a presents evolution of contact pressure. A characteristic distribution of pressure is observed for $t \geq 100$ s which results from elastic contact interaction of the ball with a nearly cylindrical groove. The pressure profile is uniform along the direction perpendicular to the sliding direction, except at the outer edge where a small pressure spike is formed. This pressure distribution is shown in detail in Fig. 15c. At the initial stage, the pressure evolves from the Hertzian distribution towards the characteristic distribution discussed above. An intermediate distribution corresponding to $t = 50$ s is shown in Fig. 15b.

It has already been mentioned that the additional computational cost related to the application of the implicit time integration scheme is small in the present example. This is because the number of additional unknowns associated with the shape transformation mapping is small compared to the

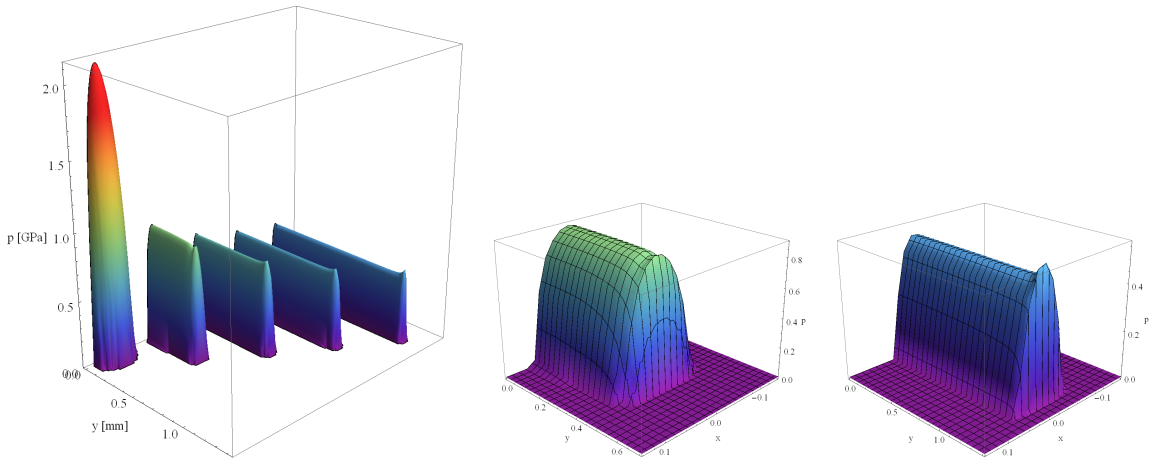

(a) (b) (c)

Figure 15: Rigid ball–elastic half-space problem, small-deformation regime: (a) evolution of contact pressure (subsequent graphs correspond to $t = 0, 50, 200, 500, 1000$ s); detailed view of contact pressure at (b) $t = 50$ s and (c) $t = 1000$ s.

total number of unknowns (less than 2%). The benefit due to stability of the integration scheme is thus obvious. Specifically, it has been checked that the critical time increment of the explicit scheme is not greater than 0.5–1 s in the present example, thus at least 1000–2000 time steps would be needed to obtain a stable solution using the explicit scheme. The corresponding computational cost would thus be approximately two orders of magnitude higher than that of the implicit scheme.

5. Conclusion

An incremental solution strategy employing the implicit backward-Euler time integration scheme has been developed for finite-deformation finite-wear problems. The advantage is that arbitrarily large time increments can be used for the incremental solution of the shape evolution problem, in contrast to the commonly used explicit scheme which is only conditionally stable. In fact, the critical time increment of the explicit scheme may be prohibitively small in practical problems, as illustrated by the numerical examples. Hence, the implicit scheme, though more involved, appears beneficial, particularly when the elastic strains are small, i.e., the elastic modulus is high in relation to the loading.

Application of the implicit integration scheme implies that the time-dependent shape transformation mapping is an additional unknown so that the size of the problem is increased. It has been demonstrated that the associated increase of the computational cost of one time step can be fully compensated by a significant reduction of the number of time steps.

In practical terms, at each time step, the problem is solved simultaneously for the nodal positions and displacements, hence the formulation is of the arbitrary Lagrangian-Eulerian type. In the present approach, the nodal positions are determined by solving an auxiliary elasticity problem. The number of the corresponding additional unknowns can be reduced by constraining the shape transformation mapping away from the contact zone. Furthermore, when the wear groove is uniform along the sliding direction, then the shape transformation mapping is prescribed at one cross-section only, and the number of additional unknowns is, in practice, negligible.

The present finite-element implementation is restricted to quasi-steady-state rigid-deformable wear problems. The potential benefit of applying the implicit scheme has been clearly demonstrated for representative examples of this class of problems. Further work on extension of the formulation to multi-body contact and to a more general class of wear problems seems thus to be a promising research topic.

Acknowledgement

This research was supported by the EU FP7 Project "Micro and Nanocrystalline Functionally Graded Materials for Transport Applications" (MATRANS) under Grant Agreement no. 228869. The author would like to thank Jakub Lengiewicz (IPPT, Warsaw) for his valuable comments and contributions at an early stage of this work.

References

[1] M. Peigney, Simulating wear under cyclic loading by a minimization approach, Int. J. Sol. Struct. 41 (2004) 6783–6799.

[2] I. Paczelt, Z. Mróz, On optimal contact shapes generated by wear, Int. J. Num. Meth. Engng. 63 (2005) 1250–1287.

[3] G. K. Sfantos, M. H. Aliabadi, Application of BEM and optimization technique to wear problems, Int. J. Sol. Struct. 43 (2006) 3626–3642.

[4] I. I. Argatov, Asymptotic modeling of reciprocating sliding wear with application to local interwire contact, Wear 271 (2011) 1147–1155.

[5] L. Johansson, Numerical simulation of contact pressure evolution in fretting, Trans. ASME J. Tribol. 116 (1994) 247–254.

[6] P. Podra, S. Andersson, Simulating sliding wear with finite element method, Tribol. Int. 32 (1999) 71–81.

[7] M. Oqvist, Numerical simulations of mild wear using updated geometry with different step size approaches, Wear 249 (2001) 6–11.

[8] I. R. McColl, J. Ding, S. B. Leen, Finite element simulation and experimental validation of fretting wear, Wear 256 (2004) 1114–1127.

[9] V. Hegadekatte, N. Huber, O. Kraft, Modeling and simulation of wear in pin on disc tribometer, Tribol. Lett. 24 (2006) 51–60.

[10] C. Paulin, S. Fouvry, C. Meunier, Finite element modelling of fretting wear surface evolution: Application to a Ti–6Al–4V contact, Wear 264 (2008) 26–36.

[11] J. Lengiewicz, S. Stupkiewicz, Continuum framework for finite element modelling of finite wear, Comp. Meth. Appl. Mech. Engng. 205–208 (2012) 178–188.

[12] I. Serre, M. Bonnet, R. M. Pradeilles-Duval, Modelling an abrasive wear experiment by the boundary element method, C. R. Acad. Sci. Paris, Serie II b 329 (2001) 803–808.

[13] G. K. Sfantos, M. H. Aliabadi, Wear simulation using an incremental sliding Boundary Element Method, Wear 260 (2006) 1119–1128.

[14] L. Rodriguez-Tembleque, R. Abascal, M. H. Aliabadi, Anisotropic wear framework for 3D contact and rolling problems, Comp. Meth. Appl. Mech. Engng. 241–244 (2012) 1–19.

[15] L. Gallego, B. Fulleringer, S. Deyber, D. Nelias, Multiscale computation of fretting wear at the blade/disk interface, Tribol. Int. 43 (2010) 708–718.

[16] J. Andersson, A. Almqvist, R. Larsson, Numerical simulation of a wear experiment, Wear 271 (2011) 2947–2952.

[17] S. Stupkiewicz, J. Lengiewicz, J. Korelc, Sensitivity analysis for frictional contact problems in the augmented Lagrangian formulation, Comp. Meth. Appl. Mech. Engng. 199 (2010) 2165–2176.

[18] N. Strömberg, An augmented Lagrangian method for fretting problems, Eur. J. Mech. A/Solids 16 (1997) 573–593.

[19] F. Jourdan, A. Samida, An implicit numerical method for wear modeling applied to a hip joint prosthesis problem, Comp. Meth. Appl. Mech. Engng. 198 (2009) 2209–2217.

[20] H. Ben Dhia, M. Torkhani, Modeling and computation of fretting wear of structures under sharp contact, Int. J. Num. Meth. Engng. 85 (2011) 61–83.

[21] M. Jean, The non-smooth contact dynamics method, Comp. Meth. Appl. Mech. Engng. 177 (1999) 235–257.

[22] T. A. Laursen, Computational Contact and Impact Mechanics, Springer-Verlag, Berlin, 2002.

[23] P. Wriggers, Computational Contact Mechanics, Springer, Berlin Heidelberg New York, 2nd edition, 2006.

[24] U. Nackenhorst, The ALE-formulation of bodies in rolling contact. Theoretical foundations and finite element approach, Comp. Meth. Appl. Mech. Engng. 193 (2004) 4299–4322.

[25] P. Alart, A. Curnier, A mixed formulation for frictional contact problems prone to Newton like solution methods, Comp. Meth. Appl. Mech. Engng. 92 (1991) 353–375.

[26] G. Pietrzak, A. Curnier, Large deformation frictional contact mechanics: continuum formulation and augmented Lagrangian treatment, Comp. Meth. Appl. Mech. Engng. 177 (1999) 351–381.

[27] J. Korelc, Multi-language and multi-environment generation of nonlinear finite element codes, Engineering with Computers 18 (2002) 312–327.

[28] J. Korelc, Automation of primal and sensitivity analysis of transient coupled problems, Comp. Mech. 44 (2009) 631–649.

[29] J. Lengiewicz, J. Korelc, S. Stupkiewicz, Automation of finite element formulations for large deformation contact problems, Int. J. Num. Meth. Engng. 85 (2011) 1252–1279.

[30] E. A. de Souza Neto, D. Perić, M. Dutko, D. R. J. Owen, Design of simple low order finite elements for large strain analysis of nearly incompressible solids, Int. J. Sol. Struct. 33 (1996) 3277–3296.

[31] J. C. J. Schellekens, R. de Borst, On the numerical integration of interface elements, Int. J. Num. Meth. Engng. 36 (1993) 43–66.